Computers and Geotechnics 167 (2024) 106092

Contents lists available at ScienceDirect

Computers and Geotechnics

journal homepage: www.elsevier.com/locate/compgeo

Research paper

Discrete element modeling of rock-filled gabions under successive boulder impacts

G.C. Yang [a], F. Qiao [a], Y. Lu [b,c,*], Q.H. Yao [a], C.Y. Kwok [c]

[a] School of Aeronautics and Astronautics, Sun Yat-sen University, Guangzhou 510275, China
[b] Department of Civil Engineering, Chu Hai College of Higher Education, Hong Kong, China
[c] Department of Civil Engineering, The University of Hong Kong, Haking Wong Building, Pokfulam Road, Hong Kong

ARTICLE INFO

Keywords:
Discrete element
Gabion
Barrier
Crushable particle
Irregular shape

ABSTRACT

A discrete element model consisting of irregular crushable filling particles and a flexible wire mesh is established. The numerical model is validated against the static net punching test and the dynamic pendulum impact test to ensure that the large irreversible plastic deformations and the impact forces during successive impacts can be captured. The impact force reduces at small friction coefficients, which is associated with the significant particle rearrangement during the impact process. The important role of friction is further confirmed by the energy evolution, showing that friction is the dominant mechanism for energy dissipation, instead of the more intuitionistic collision or particle crushing. Besides, the increase of impact force with the number of impacts becomes more significant at a higher impact energy due to the faster rate of momentum exchange. A bounce-back behavior of the boulder is observed when the impact energy is low, which may attenuate the impact force like the reflection waves in real debris flow events where multiple boulders are present. Our results highlight the combined effects of contact properties and impact energy, which are valuable in the design of rigid barriers shielded by rock-filled gabions for hazard mitigation in engineering practice.

1. Introduction

Debris flows are well known for their destructive nature, usually bringing huge economic losses and heavy casualties. Debris flows are composed of polydisperse soil particles and water, flowing downslope rapidly under the influence of gravity in the form of multiple surges. As a result of the heterogeneous flow architecture, particle-size segregation plays an important role in the transport and deposition processes and results in unique features of debris flows, including the formation of bouldery fronts and levees (Iverson, 1997; Johnson et al., 2012). To mitigate debris flow hazards, protection works are usually installed along the flow path for interception (Hübl et al., 2009; Volkwein et al., 2011; Vagnon, 2020; Huang and Zhang, 2022). Therefore, understanding the underlying mechanisms of the complex flow-structure interactions for the better prediction of impact force becomes the key to guide more efficient and economic engineering design of countermeasures.

Rigid barriers are large geotechnical structures installed at the downstream of debris flow gullies. In practice, rigid barriers are sometimes shielded by gabions, which are cellular structures fabricated from interconnected wire mesh baskets and filled with rock fragments (see Fig. 1). The function of gabions is to diffuse the concentrated impact forces from the fast moving boulders and to absorb kinetic energies, thereby reducing the force transmitted to the back rigid wall. According to the large scale pendulum impact test carried out by Ng et al. (2016), the maximum impact force estimated from the theoretical Hertz equation can be seven times larger than the measured value when a gabion cushion layer is applied. In addition, due to the cellular nature of gabions, maintenance work can be easily performed by repairing or replacing the damaged baskets (Lambert et al., 2014).

However, characterizing the mechanical response of the gabion cushion layer under impacts is nontrivial (Bertrand et al., 2005; Bertrand, 2008). On one hand, the wire mesh baskets provide confinement to the filling granular materials; on the other hand, the rock fragments provide internal resistance to external loadings and dissipate energy via large plastic deformations. Many experiments have been conducted to investigate the effectiveness of the gabion cushion layer. Lambert et al. (2009) performed a series of impact tests by dropping a spherical boulder onto a single cubic gabion and found that coarse filling materials are more effective for reducing the impact force due to particle crushing. Also, the boundary condition can make a significant influence and the lowest impact force was found when the gabion was free-to-deform laterally. Later on, a real-scale embankment protected by two

* Corresponding author at: Department of Civil Engineering, Chu Hai College of Higher Education, Hong Kong, China.
E-mail address: helenlu@chuhai.edu.hk (Y. Lu).

https://doi.org/10.1016/j.compgeo.2024.106092
Received 29 May 2023; Received in revised form 8 January 2024; Accepted 9 January 2024

Fig. 1. The urban area is separated from the natural terrain by a huge gabion shielded concrete wall to prevent debris flow hazards.
Source: This picture was taken in 2018 during a site visit to Yu Tung Road, Hong Kong.

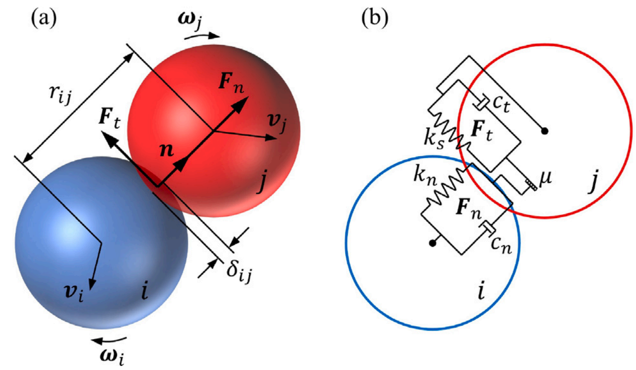

Fig. 2. (a) Sketch of two interacting balls: ball i in blue and ball j in red. (b) Sketch of the spring–dashpot model for the calculation of normal ($\boldsymbol{F}_n$) and tangential ($\boldsymbol{F}_t$) contact forces between two interacting balls.

layers made from gabions filled with either stones or a sand-shredded-tire mixture was constructed by Lambert et al. (2014) to study the deformation and the dynamic responses under impacts. Large-scale pendulum impact tests were performed by Ng et al. (2016), focusing on the performance and robustness of gabion shielded rigid barriers under successive boulder impacts, which is commonly encountered in real debris flow events. Design procedures for the gabion shielded rigid barriers have also been proposed according to the experimental results from the large-scale pendulum impact tests (Perera et al., 2021; Perera and Lam, 2023).

As an alternative to expensive field tests, numerical models have been developed to predict the impact force and the penetration depth for the design of the gabion cushion layer. Although continuum methods can be applied to analyze the energy absorption capacity of cushion materials with the use of a proper constitutive law (Coelho et al., 2013; Brocato, 2020), a complicated remeshing algorithm has be to implemented to account for large deformations (Breugnot et al., 2016). Even so, the particle crushing at the impact vicinity and the local evolution of contact force chains in a granular assembly still cannot be easily reproduced using continuum approaches. Therefore, the Discrete Element Method (DEM) has been extensively applied for the numerical analysis of the cushion performance of rock filled gabions, despite its relatively larger computational cost (Bertrand, 2008; Breugnot et al., 2016; Su et al., 2019, 2021; Su and Choi, 2021). Bertrand et al. (2005), Bertrand (2008) simulated a granular media confined by a metal wire mesh explicitly using DEM. The calibrated model was able to reproduce the force development in both quasi-static and dynamic loading conditions. A hybrid approach coupling the finite difference method and DEM was adopted by Breugnot et al. (2016) to simulate the small and large deformation areas of a real-scale embankment shielded by rock filled gabions under boulder impacts in an accurate and efficient manner. Besides, parametric studies of particle size, particle shape, cushioning thickness and particle crushing strength altering the mechanical response of rock-filled gabions under boulder impacts have been carried out (Bourrier et al., 2011; Su et al., 2019, 2021; Su and Choi, 2021).

Up to now, many numerical simulations and experiments focus on the performance of the gabion cushion layer under one single boulder impact, although successive impacts that can be caused by multiple surges of debris flows seem to be the more realistic loading pattern (Heymann et al., 2010; Ng et al., 2016; Perera and Lam, 2023; Yan et al., 2023). Here we carry out DEM simulations of rock-filled gabions under successive boulder impacts, as a supplementary study to the experimental work conducted by Ng et al. (2016). DEM modeling allows us to get access to additional information (e.g., energy dissipations due to different mechanisms) that cannot be easily measured in experiments, and to investigate the effects of micro-mechanical parameters (e.g., inter-particle friction coefficient and damping ratio). The impact energy is also varied to examine its influence on the cushioning performance and how it deteriorates as the number of impacts increases.

This paper is organized as follows. Section 2 presents the detailed numerical techniques to simulate rock-filled gabions using DEM, together with a simplified model setup resembling the large-scale pendulum impact test. The numerical model is validated against the experimental measurements (both forces and deformations) in Section 3. Then, the effects of the contact properties and the impact energy are discussed in Section 4. Conclusions are drawn in Section 5.

2. Numerical configuration

2.1. Discrete element method

All numerical simulations in this study are run using the Itasca software PFC3D (Particle Flow Code in three dimension), which is based on the widely used discrete element method (DEM) for the simulation of granular materials (Cundall and Strack, 1979). In the classic formulation of soft-sphere DEM, the dynamics of each individual ball is tracked following Newton's second law of motion. Balls are treated as non-deformable rigid bodies that can translate and rotate, but with soft contacts allowing small overlaps between interacting objects, see Fig. 2(a). The overlap between spherical balls i and j is easy to calculate:

$$\boldsymbol{\delta}_{ij} = (r_i + r_j - r_{ij})\boldsymbol{n}, \tag{1}$$

where r_i and r_j are the radii of balls i and j, respectively. The spacing between the ball centers is denoted as r_{ij} and $\boldsymbol{n}$ is the unit normal along the line connecting the ball centers. Note that in this study we specifically use ball to denote the spherical element in DEM and use particle to denote the rock fragment inside the gabion.

In this study, three different contact models have been adopted to calculate the contact forces: (i) the linear parallel bond model (Potyondy and Cundall, 2004) is installed at ball–ball contacts if both interacting balls belong to the same rock particle inside the gabion; (ii) the soft bond model (Ma and Huang, 2018) is installed at ball–ball contacts if both interacting balls belong to the wire mesh constituting the gabion; (iii) the linear model is installed at any other ball–ball contacts and all ball–wall contacts. Details of the first two contact models for the simulation of crushable rock particles and wire mesh will be introduced in Sections 2.2 and 2.3. As for the linear model, the contact forces can be calculated based on a simple spring–dashpot model (Cundall and Strack, 1979), as shown in Fig. 2(b). The normal contact force $\boldsymbol{F}_n$ is given by:

$$\boldsymbol{F}_n = k_n\boldsymbol{\delta}_n - c_n\boldsymbol{\Delta u}_n, \tag{2}$$

where k_n and c_n are the stiffness and the damping coefficient in the contact normal direction. The relative normal velocity is denoted by $\boldsymbol{\Delta u}_n$. The tangential contact force $\boldsymbol{F}_t$ is written as:

$$\boldsymbol{F}_t = -k_t \int_{t_{c,0}}^{t_c} \boldsymbol{\Delta u}_t \, dt - c_t \boldsymbol{\Delta u}_t, \tag{3}$$

where k_t and c_t are the stiffness and damping coefficient in the tangential direction and the relative tangential velocity is denoted by $\boldsymbol{\Delta u}_t$. The integral corresponds to an incremental spring that stores energy from the relative tangential motion over the contact duration from $t_{c,0}$ to t_c. The negative signs on the right hand side of Eq. (3) indicate that the tangential force points to a direction opposite to the tangential displacement. The two contacting balls will slide against each other when the magnitude of the tangential force reaches the Coulomb friction μF_n, where μ is the smaller friction coefficient of the two balls in contact. The model parameters (k_n, k_t, c_n, c_t) are constants defining the material properties that can be measured directly or indirectly. In PFC3D, the damping coefficients (c_n and c_t) are set by the critical damping ratios (β_n and β_t), which are required to account for the energy loss due to collisions. The damping ratio can be further converted to the restitution coefficient by $\exp(-\beta_n \pi / \sqrt{1-\beta_n^2})$ in the normal direction, and a value of $\beta_n = 0.1$ gives a restitution coefficient close to 0.73 during a drop test.

Based on the contact forces, a resultant torque ($\boldsymbol{T}_c$) acting on a ball can be calculated. Then, its translational and rotational velocities can be updated according to Newton's second law of motion:

$$m\boldsymbol{a} = \boldsymbol{F}_t + \boldsymbol{F}_n + \boldsymbol{G}, \tag{4a}$$

$$I\dot{\boldsymbol{\omega}} = \boldsymbol{T}_c, \tag{4b}$$

where m and I are the mass and the moment of inertia of the ball. The symbols $\boldsymbol{a}$ and $\boldsymbol{\omega}$ denote the acceleration and angular velocity, respectively. An explicit scheme is adopted to integrate Eq. (4) over a small time step to update the ball positions and orientations.

2.2. Discrete element modeling of filling materials

One of the difficulties to capture the mechanical responses of rock-filled gabions is the irregular shape of the filling particles combined with their crushable nature under large impact forces. Following Su et al. (2021), each rock particle is generated by aggregating balls using the linear parallel bond model, which is a popular approach to model crushable materials (Potyondy and Cundall, 2004). The linear parallel bond model in PFC consists of two parts: one is the linear model introduced in Section 2.1, which is still active if there exists a positive overlap δ_{ij}; the other is the parallel bond based on the classic beam theory, which can be visualized as a series of elastic springs distributed over a finite contact area between two interacting balls (Potyondy and Cundall, 2004). Different from the linear model, the parallel bond can resist both tension and bending moment. The normal and tangential contact forces, $\bar{F}_n$ and $\bar{F}_t$, and the bending moment ($\bar{M}$) are calculated in an incremental form:

$$\Delta\bar{F}_n = \bar{k}_n \bar{A} \Delta\bar{\delta}_n, \quad \Delta\bar{F}_t = -\bar{k}_t \bar{A} \Delta\bar{\delta}_t, \quad \Delta\bar{M} = -\bar{k}_n \bar{I} \Delta\bar{\theta}, \tag{5}$$

where the symbols with a bar above are quantities associated with the bond model. The normal and shear stiffnesses per unit area are denoted by $\bar{k}_n$ and $\bar{k}_t$, respectively. The contact area ($\bar{A} = \pi\bar{r}^2$) is normally defined by a radius multiplier ($\bar{\lambda}$), where $\bar{r} = \bar{\lambda}\min(r_i, r_j)$. The normal and tangential displacements are denoted by $\bar{\delta}_n$ and $\bar{\delta}_t$, respectively. The moment of inertia of the parallel bond and the relative rotation angle are denoted by $\bar{I}$ and $\bar{\theta}$, respectively.

Note that $\Delta\bar{F}_n$ and $\Delta\bar{\delta}_n$ are assumed to be positive when the parallel bond is stretched, and the corresponding stress–strain behavior is presented in Fig. 3. There exists a maximum tensile stress or a bond strength (σ_{max}) that delimit the elastic state and the broken state (the normal stress immediately drops to zero when σ_{max} is reached, see the blue dashed line in Fig. 3). Also, the parallel bond is unrecoverable

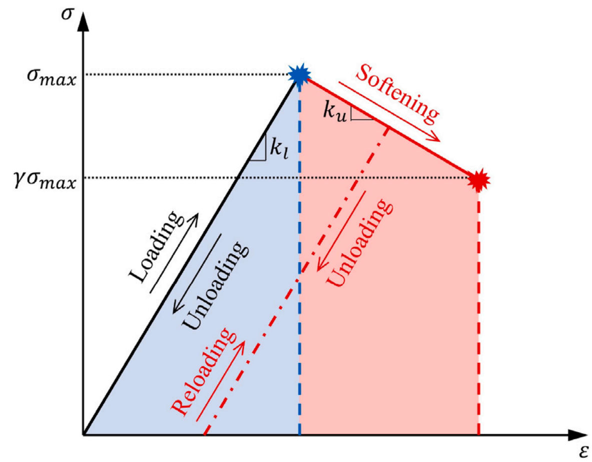

Fig. 3. Comparison between the linear parallel bond model and soft bond model regarding the stress–strain relationship under loading and unloading when the bond is stretched. The blue and red lines indicate the stress–strain behaviors of the linear parallel bond model and the soft bond model, respectively, after the strength σ_{max} is reached.

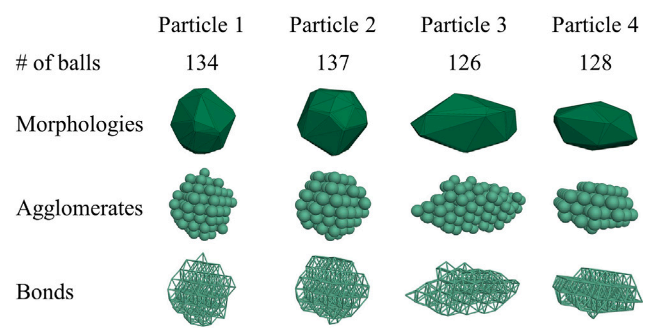

Fig. 4. Four crushable particles (or agglomerates) in different shapes formed by bonding balls using the linear parallel bond model.

once breakage has occurred. A similar behavior can be observed if the parallel bond is sheared or bended.

In this study, crushable particles or agglomerates with irregular shapes are created by carving a big chunk of balls arranged in a hexagonal close packing (McDowell and Harireche, 2002; Cheng et al., 2003; Bolton et al., 2008). In total, there are four different shapes reconstructed using around 130 spherical balls (see Fig. 4), covering both rounded and angular morphologies to account for the complex particle shape of rock fragments. Each constituent ball has a radius of 20 mm, resulting in a total volume of 0.006 m^3 enclosed by the surface of the shape, which is roughly the average size of rock particles used in the field to construct rock filled gabions (Ng et al., 2016; Su et al., 2021). The equivalent diameter of the particles if they are in a spherical shape and with the same volume is about 225 mm, which falls in the preferred size range (from 150 mm to 300 mm) suggested by the local design guide for retaining structures (GEO, 1993). The neighboring balls are connected by the parallel bonds, forming a stable structure (similar to truss with fixed joints) that can deform and fracture under loading.

To calibrate the model parameters for the filling particles, DEM simulations of the standard uniaxial compression test are carried out. The numerical results are compared to the experimental measurements conducted by Su et al. (2021). The rock samples are in a cylindrical shape with a height and a diameter equal to 200 mm and 100 mm, respectively. The measured rock density is around 2700 kg/m^3. In the DEM simulation, a cylinder with the same dimension of the rock samples in the experiments is constructed using the same approach

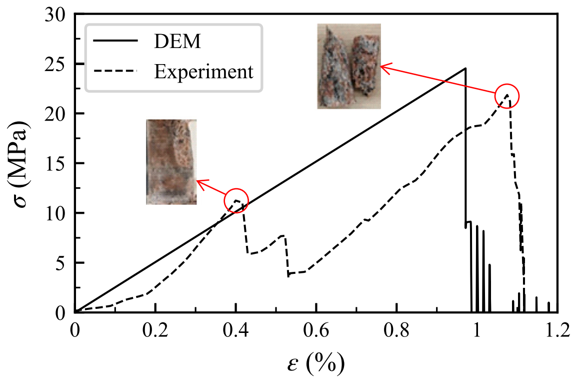

Fig. 5. Comparison between the numerical and experimental results regarding the stress–strain relationship in a standard uniaxial compression test. The experimental curve is extracted from Su et al. (2021). The insets show the minor and the major fractures of the rock sample under compression, which are responsible for the significant drops of the measured stress–strain curve.

for creating crushable filling particles, as shown in Fig. 4. The model parameters requiring calibration include the stiffnesses and the normal-to-shear stiffness ratios for the contact and the parallel bond, the bond strength (σ_{max}), the normal and tangential damping ratios (β_n and β_t), and the friction coefficient (μ). To reduce the number of calibration parameters, it is assumed that the ball–ball contact and the parallel bond share the same elastic properties such that their stiffnesses can be defined by a single Young's modulus E, which can be converted to the normal stiffnesses via $k_n = EA/L$ and $\bar{k}_n = E/L$. The parameters A and L denote an area and a length, respectively. For ball–ball contacts, $A = \pi r^2$ and $L = r_i + r_j$, where r_i and r_j are the radii of the two contacting balls and $r = \min(r_i, r_j)$. For ball-wall contacts, the area A still equals to πr^2 but both L and r are defined as the radius of the particle.

Fig. 5 presents the typical stress–strain behavior of a rock sample under compression. To match the experimental measurements, the Young's modulus and the normal-to-shear stiffness ratio are set to be 1.0 GPa and 2.0, respectively. The bond strength (σ_{max}) is set to be 6 MPa. The friction coefficient (μ) and the damping ratios (β_n and β_t) are set to be 0.3 and 0.1, respectively. Note that multiple drops of the measured stress–strain curve before the major failure are observed, which are caused by the minor fractures, see the inset of Fig. 5. Such minor fractures are likely related to the variability of strength introduced by the internal flaws and discontinuities in natural rocks. Since the DEM model consists of a regular packing of spherical balls and no variability is applied to the bonding strength, the compressive stress increases almost linearly until a major failure occurs. All in all, the calibrated DEM model agrees with the experiment fairly well regarding the macroscopic stiffness and the peak strength. Note that the stress–strain behavior corresponding to the lowest uniaxial compressive strength measured by Su et al. (2021) has been taken for calibration to account for the possible degradation of the filling materials due to weathering, crushing, and abrasion. Readers are referred to Su et al. (2021) for the combined effect of crushing strength and particle shape. In Section 4.1 of the current work, the values for the friction coefficient and the damping ratios are varied to examine their influence on the impact characteristics of rock filled gabions.

2.3. Discrete element modeling of wire mesh

Two modeling strategies have been adopted to simulate wire meshes using DEM successfully, referring to the wire-node method (Bertrand et al., 2005, 2006; Nicot et al., 2007; Bertrand, 2008; Bertrand et al., 2008; Li and Zhao, 2018; Pol et al., 2021) and the wire-cylinder method (Bourrier et al., 2013; Albaba et al., 2017; Effeindzourou et al., 2017; Marigo et al., 2021). The former describes the wire mesh by a collection of balls at nodes linked by remote interaction forces, such as the parallel bond introduced in Section 2.2. The latter simulates the wire mesh explicitly by means of interconnected cylinders. Here, we choose to use the wire-node approach, which allows the use of nodal balls larger than the wire mesh, resulting in a better performance in computational efficiency.

When the wire-node method is adopted, the strength of wire mesh to resist compression and bending is usually ignored by assuming an immediate onset of buckling (Thoeni et al., 2013). However, this assumption may lead to noticeable errors when the wire cross-section enlarges. In this study, a soft bond contact model that can resist both tension and compression is adopted to capture the mechanical response of each wire mesh element (one segment between two nodal balls). Similarly to the parallel bond model, the soft bond fails if the bond strength is exceeded either in shear or in tension. In addition, the soft bond model has the ability to account for the potential irreversible plastic deformation of the wire mesh under loading. The softening stress–strain behavior is implemented into the normal component of the contact, which is plotted in Fig. 3. Compared to the parallel bond model, a softening stage exists after σ_{max} is reached and before bond breakage. The normal displacement during the softening stage can be calculated as (Ma and Huang, 2018):

$$\bar{\delta}_n = \frac{\sigma_{max}}{\bar{k}_n} + \frac{\sigma_{max} - \bar{F}_n/\bar{A}}{\zeta \bar{k}_n}, \tag{6}$$

where ζ is the softening factor defined as the ratio between the loading and softening stiffnesses, i.e., $\bar{k}_l = \zeta \bar{k}_u$ and $\bar{k}_l = \bar{k}_n A$. An additional tensile strength factor γ, which varies between 0 and 1, is applied to define a critical stress level ($\gamma\sigma_{max}$) for the bond breakage. When the softening factor ζ approaches 0 or the tensile strength factor γ approaches 1, the soft bond behaves just like the parallel bond, which is associated with a brittle failure behavior.

To test the performance of the soft bond model for the simulation of wire mesh, DEM simulations of the standard net punching test are carried out. Fig. 6(a) shows the geometries of the wire mesh and the punching element, which are set according to the experiments conducted by Pol et al. (2021). A square mesh panel of dimensions 3 m by 3 m, which consists of a set of interconnected hexagonal cells, is simulated. Each hexagonal cell is composed of single wires (oriented in ±45° to the horizontal direction) and double-twisted wires (oriented vertically). The dimensions in the horizontal and vertical directions of a hexagonal cell are measured to be 8 cm and 12 cm, respectively. The punching element is in the shape of a spherical dome with a diameter $D = 1.0$ m and a curvature radius $R = 1.2$ m. The dune edge is rounded with a curvature radius of 0.05 m.

Following Previtali et al. (2020), a mesh sensitivity analysis is performed and three different resolutions have been tested using $N = 2$, 3, 4 balls to construct the single and the double-twisted wires, as shown in Fig. 6(b). To save the computational cost, the diameter of the nodal balls is set to be $d_n = 10.8$ mm, which is four times of the actual wire diameter (Pol et al., 2021), so the radius multiplier becomes $\bar{\lambda} = 0.25$. In this study, it is assumed that the single wire and the double-twisted wire share exactly the same material and contact properties, except that the cross-sectional area of the double-twisted wire is doubled. This simplification is considered to be more acceptable based on the fact that the single and the double-twisted wires behave similarly in a tensile test regarding the stress–strain relationship (Thoeni et al., 2013; Pol et al., 2021). As a result, the number of model parameters for calibration is reduced. The density of nodal balls depends on the resolution and it is set so that the total weight equals to the actual mesh panel and thus maintains the inertia. In DEM simulations, the macroscopic mechanical response is determined by the microscopic contact properties. To match the experimental measurements, the Young's modulus and the Poisson's ratio are set to be 12.5 GPa and 0.3, respectively. Note that the calibrated Young's modulus is about one order of magnitude smaller

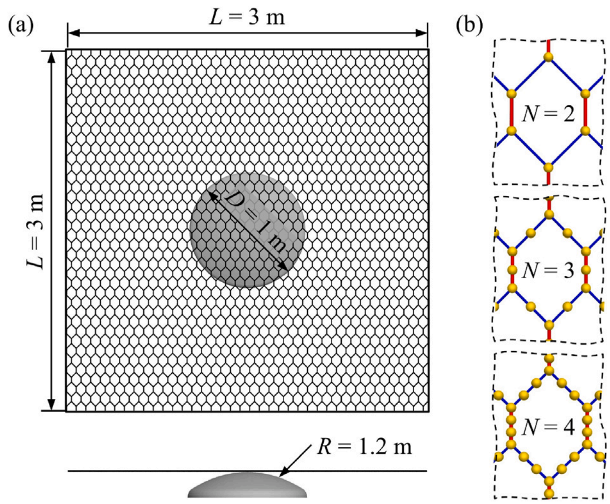

Fig. 6. Net punching test. (a) Geometries of the mesh panel and the punching element. (b) Sketches of the double-twisted hexagonal wire mesh with segments simulated using 2, 3, and 4 balls. The red and blue segments represent the double-twisted and single wire, respectively.

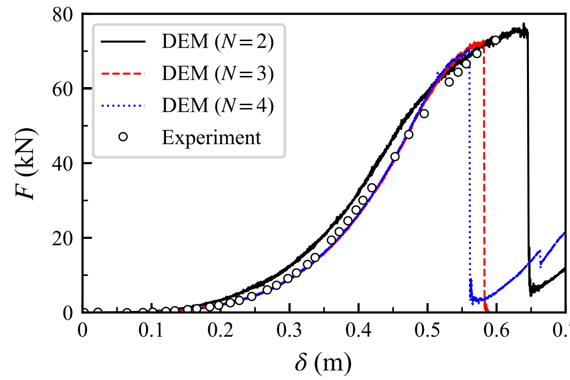

Fig. 7. Comparison between the numerical and experimental results regarding the force–displacement relationship in a standard net punching test. The experimental data is measured by Thoeni et al. (2013).

than the actual property of mesh wires (Bertrand et al., 2008). It is due to the fact that the soft bond model assumes an elastic response of the mesh wire before failure so that the resulting Young's modulus becomes an apparent value, which should not be taken as the intrinsic material property. Generally speaking, the apparent Young's modulus reduces as the deformation increases. The tensile strength σ_{max} of the soft bonds is set to be 520 MPa. The softening factor ζ and the tensile strength factor γ are set to be 200 and 0.9, respectively. The friction coefficient is set to be 0.1.

A constant velocity of 0.1 m/s is assigned to the punching element in the out-of-plane direction of the mesh panel. Note that a larger loading velocity is applied in the DEM simulations compared to the experiments, which does not alter the results significantly and saves computation time (Pol et al., 2021). The translational displacement of the nodal balls at the outer boundary is inhibited to mimic the fixed boundary condition in the experiment. The total force acting on the punching element is plotted against the displacement in Fig. 7. All simulations are run for 0.7 s, before which a major failure to the mesh panel takes place indicated by the sudden drop of loading force. In general, the influence of the resolution N on the mechanical response of the mesh panel is small. A slightly stiffer response and a higher peak force before failure are observed when $N = 2$, which is commonly applied in literature. The force–displacement curves from DEM simulations with $N = 3$ and $N = 4$ almost overlap and agree with the experimental data. Since the soft bond model allows bending moment to develop within the virtual wire strands based on Eq. (5), a large influence of N is expected if bending is the dominant mechanism due to the higher degree of freedom introduced by the insertion of additional nodal balls. Meanwhile, the small influence of N in the actual simulation demonstrates that the wire strands are mainly exposed to tensile loading during the punching test and bending is a negligible mechanism. In the following simulation of a rock filled gabion, a mesh resolution of $N = 3$ is adopted. Note that using a smaller resolution of $N = 2$ shall be totally viable due to its small influence, if the computational efficiency is of major concern. Also, compared to the numerical results from the parallel bond model (Previtali et al., 2020), our results show that the soft bond model seems to be able to better reproduce the mechanical response of the mesh panel, especially regarding the reduced out-of-plane stiffness before the failure. Finally, although fair results have been obtained with the simplified DEM model in this study, the difference between the single and the double-twisted wires should not be overlooked when their stress–strain relationships become very different (Bertrand et al., 2008). In such cases, it is suggested that the contact properties for the single and the double-twisted wires should be calibrated against experimental measurements separately.

2.4. Model setup for rock-filled gabion

To study the cushion performance of rock-filled gabions, we perform one-to-one numerical simulation of the large-scale pendulum impact test conducted by Ng et al. (2016). In the experiment, a gabion cushion layer is installed in the front of a heavy concrete wall (around 32.4 tones), which is 3 m in length, 3 m in width and 1.5 m in thickness. Nine cubical gabion cells are stacked together in a 3-by-3 pattern, forming the gabion cushion layer of 3 m in length, 3 m in width and 1.0 m in thickness. Each gabion cell is filled with granitic fragments and weights about 15 kN. The gabion baskets are made of hexagonal woven wire meshes with a wire diameter of 2.7 mm, which is the same size of the single wire used in the net punching test (see Section 2.3). Thus, the same properties of the single wire in the punching test are adopted here for the simulation of the wire mesh. A large spherical concrete boulder with a diameter and a mass of 1.16 m and 2000 kg, respectively, is connected to a fixed frame using steel strand cables, which can be lifted up and released at different heights to initiate a sway motion before impacting on the gabion cushion layer and the rigid concrete wall. The details of the test procedures and the instrumentations are available in the Ref. Ng et al. (2016).

There are mainly four steps to build a DEM model for rock-filled gabions under successive boulder impacts, as shown in Fig. 8. First, a box bounded by rigid walls and in the shape of the entire gabion cushion layer is filled with the four types of particles presented in Fig. 4. In total, there are 732 number of particles, corresponding to 183 particles per each type. The resulting packing fraction is about 0.49 and the unit weight of the gabion cushion layer is around 13 kN/m^3, which is smaller than the value (i.e., 15 kN/m^3) in the experiment (Ng et al., 2016). The reason is twofold. First, the filling particles are stacked manually by human so that the particles can be better aligned to achieve a higher packing density. Such a manual process is rather difficult to be replicated in any numerical simulation. It is only possible if the grain skeleton is provided, which requires advanced scanning techniques and is rarely performed even in small-scale elementary tests. Therefore, a random packing is adopted in this work, resulting in a relatively looser state. Second, the packing density also depends on the particle shape and particle size distribution. The detailed particle information is not available and the related model parameters are estimated according to the local guidelines (GEO, 1993) and visual examinations of the

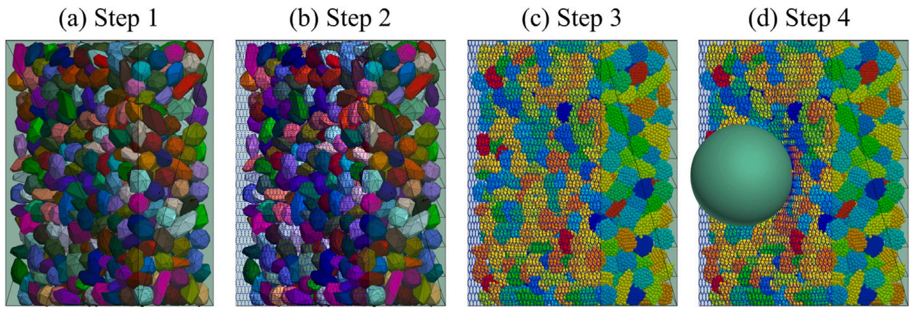

Fig. 8. Procedures to setup a DEM model for rock-filled gabions under successive boulder impacts. (a) Step 1: fill the box bounded by rigid walls with clumps. (b) Step 2: replace the front wall with nodal balls for the wire mesh and subdivide the back wall. (c) Step 3: convert clumps to agglomerates and bond the nodal balls for the wire mesh. (d) Step 4: impact the agglomerates and the wire mesh with a boulder.

experimental condition (Ng et al., 2016) to instantiate our simulation. Also, to study the potential mass effect in such a dynamic problem, a sensitivity analysis has been performed by increasing the particle density to match the unit weight of the experimental value and the result (not shown here) indicates that the reduction of unit weight from 15 kN/m^3 to 13 kN/m^3 only has a small effect on the mechanical response. The small mass effect is likely due to the fact that the gabion cushion layer is well confined by the rigid walls during the whole impact process. Note that the clump logic is used here so that all balls within one particle moves together following a rigid body motion (de Bono and McDowell, 2016).

Second, the front wall (facing left) is replaced with nodal balls for the wire mesh and all the other walls remain rigid to mimic the surrounding steel frames and the thick concrete (back) wall in the physical experiment (Ng et al., 2016). To prevent the mesh panel from moving during impacts, the translational velocities of the balls at the edges are fixed to be zero. Previous real-scale experiments on gabion structures subjected to boulder impacts have shown that the tensile resistance introduced by the wire mesh baskets has the ability to provide extra confinement to the filling particles and potentially increase the zone of the structure associated with the impact response under large deformations (Lambert et al., 2014, 2020). Due to the rigid boundary conditions provided by the steel frames and the concrete wall, together with the relatively small size of the gabion cushion layer in this study, the deformations in the transverse and along the impact directions of the whole structure are limited. Therefore, the interactions between the wire meshes belonging to different gabion cells are considered as minor and are ignored in the DEM simulation. Note that the lateral confinement to the particles inside a gabion cell can still be provided by the particles in neighboring cells and the rigid boundaries. The back wall (facing right) is subdivided into 81 (i.e., 9 by 9) small squares with a length of 333 mm so that local measurements of the forces transmitted to the back wall can be conducted. Third, the clump logic is removed and balls belonging to the same particle are bonded with the linear parallel bond model, see Section 2.2. The nodal balls of the wire mesh are connected by remote interactions defined by the soft bond model, see Section 2.3.

Finally, a large particle with the same properties of the concrete boulder is created and is assigned with a initial velocity moving from left to right for the impact on the gabion cushion layer. The abovementioned DEM model for rock-filled gabions is derived from the simple box model from Su et al. (2021), in which the gabion baskets are ignored and the filling particles are simply enclosed by rigid walls. The inclusion of a layer of wire mesh facing the boulder has the advantage of capturing the complex interactions among the boulder, the wire mesh and the filling particles more accurately, which may play a major role especially when successive impacts are considered and large plastic deformations or even breakage of the wire mesh may take place (Ng et al., 2016). Note that our DEM model is still largely simplified compared to real gabions, and more sophisticated models exist in literature, e.g., the models from Effeindzourou et al. (2017) and Marigo et al. (2021).

3. Comparison between numerical and experimental results

In this section, we present the results of a one-to-one numerical simulation of the large-scale pendulum impact test carried out by Ng et al. (2016). Detailed information of the boulder impact force, the load transmitted to the rigid barrier and the deformation of the gabion cushion layer has been measured in the experiment, which will be utilized to examine the performance of our DEM model.

3.1. Impact dynamics and boulder impact force

Fig. 9(a) presents the time history of the boulder velocity. Initially, a positive velocity of 4.5 m/s moving towards the gabion cushion layer is assigned to the boulder so that the simulation mimics the condition with the impact energy equal to 20 kJ. The velocity starts to decrease as soon as the boulder touches the wire mesh and the filling particles, progressively transferring the kinetic energy of the boulder to the gabion cushion layer in the form of kinetic energy and strain energy (Lambert et al., 2009). During the impact process, a part of the energy is dissipated due to inter-particle interactions (i.e., friction and collision) and particle crushing. According to Ng et al. (2016), a maximum impact duration of 0.1 s is observed for the first impact. To ensure every impact process is fully completed, a longer impact duration of 0.2 s is simulated. After that, the boulder is moved back to its initial position with a constant velocity of 4.5 m/s. Then, the boulder is stopped and the simulation continues for another 0.1 s so that a temporary equilibrium state is obtained (see the negligible kinetic energy of particles inside the gabion in Section 4). Up to now, a full cycle of the impact simulation is finished and the gabion cushion layer is ready for the next boulder impact. In this study, the time period associated with a continuous decline of the boulder velocity is considered as one impact duration and six successive impacts in total have been simulated. Fig. 9(a) shows that the impact duration of the first impact is significantly longer than the follow-up impacts, which qualitatively agrees with the experimental measurements (Ng et al., 2016).

In DEM simulations, the boulder impact force can be calculated by the product of the boulder mass and acceleration, or by summing up the x-component of all the contact forces acting on the boulder. We have checked that both methods yield rather similar results with a minor difference. The time history of the boulder impact force is presented in Fig. 9(b). In every successive impact, the boulder impact force increases suddenly to a peak value and then gradually decreases. Interestingly, the peak impact force becomes significantly larger after the first two impacts and reaches its maximum during the last (i.e., the sixth) impact, indicating that the gabion cushion layer is densified and gradually stiffens under successive impacts. The sudden drop of the peak impact force after the third impact is attributed to the collapse of one or multiple strong force chains that originally counteract the boulder impact motion due to particle crushing and rearrangement (Tsoungui

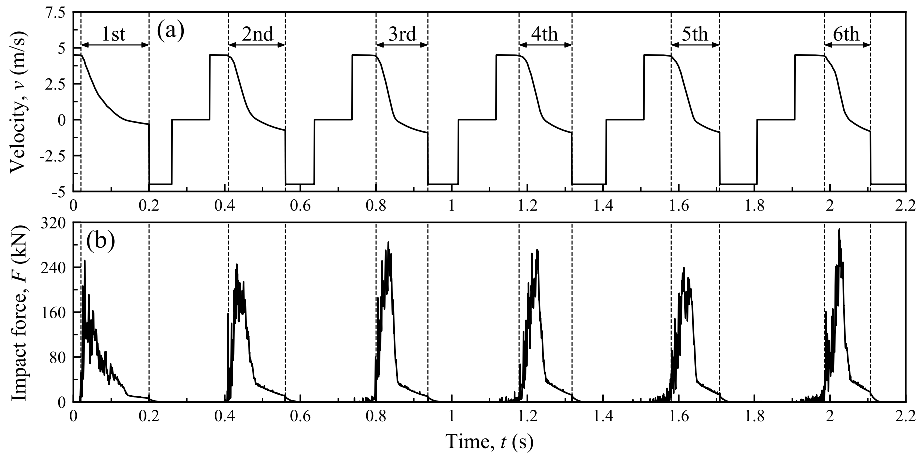

Fig. 9. Time histories of (a) the boulder velocity and (b) the impact force during six successive boulder impacts when the impact energy is 20 kJ.

et al., 1999; Zhang et al., 2017). In general, Fig. 9 shows that the larger peak impact force is associated with the shorter impact duration when the impact energy is fixed.

In the experiment, an accelerometer is attached to the back of the concrete boulder to record the deceleration so that the impact force can be calculated according to Newton's second law (Ng et al., 2016). Fig. 10 compares the numerical result and the experimental measurement regarding the temporal evolution of the boulder impact force for the first and sixth impacts. Several differences can be observed. First, the numerical result fluctuates much more than the experimental data, which can be caused by the higher data acquisition frequency in the numerical simulation. Note that the accuracy of the experimental data highly depends on the performance of the instrumentation and the sensor raw data could be post-treated (i.e., filtered or smoothed). Lambert et al. (2009) carried out a similar impact test by dropping a spherical boulder onto a cubic geocell and large fluctuations were observed for the measured impact force. Second, the curves for the time history of the measured boulder impact force are quite symmetric with nearly the same increasing and decreasing rates. Meanwhile, the numerical results show that the boulder impact force increases rapidly but decreases more gently. Finally, although the densification or stiffening effect is present in both the numerical simulation and the experiment, the corresponding peak values do not match very well. More specifically, the peak impact forces for the first and sixth impacts in the numerical simulation are 252 kN and 308 kN, respectively, which are higher and lower than the measured values, i.e., about 111 kN and 397 kN, respectively. The discrepancies between the numerical and the experimental data in terms of the boulder impact force are expected, since the size ratio between the gabion and the particle is relatively small (about 10 to 1) and a high variability of the granular fabric exists due to the finite size effect. The same problem has been encountered previously when examining the force on rock filled gabions in both static and dynamic conditions (Breugnot et al., 2016). Therefore, the comparison of experimental data with numerical results should be conducted with caution and it is more important to capture the trend, instead of matching the specific values by tuning the model parameters.

3.2. Load transmitted to the rigid barrier

The key function of the gabion cushion layer is to diffuse the concentrated impact force, and thereby reducing the load transmitted to the rigid barrier. Fig. 11 compares the numerical and experimental data regarding the spatial distribution of the maximum transmitted force for the first and sixth impacts at an energy level of 20 kJ. First, it should be noted that the magnitude of the transmitted force depends on the size of the measurement area (i.e., the load cell in the experiment). According to Ng et al. (2016), the dimension of the load cell surface

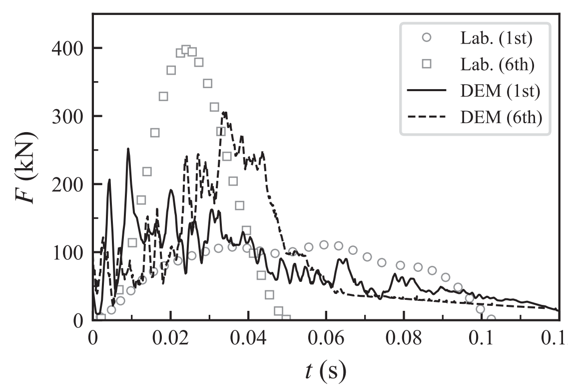

Fig. 10. Comparison between the numerical and experimental data regarding the time history of the boulder impact force for the first and the sixth impacts when the impact energy is 20 kJ. The experimental data is measured by Ng et al. (2016).

used in the experiment is 150 mm by 150 mm in length. However, the transmitted force in the numerical simulation is measured locally by a square with a length of 333 mm (see Section 2.4). Assuming the transmitted force is linearly proportional to the measurement area, we have magnified the experimental data by a factor of 4.93.

Fig. 11 shows that the transmitted force is larger close to the center of the gabion cushion layer and gradually decreases as moving outwards. The DEM result shows that the transmitted force of the sixth impact is generally larger than that of the first impact, similar to the boulder impact force as shown in Fig. 10. However, there is only a small difference observed for the measured transmitted force during the first and sixth impacts in the experiment. It is probably due to the fact that, in the experiment, the impact direction is not entirely perpendicular to the rigid barrier after the first impact due to the swaying motion of the boulder (Ng et al., 2016). As a result, the load cell only measures a component of the transmitted force, which shall be lower than the value if a perpendicular impact is enforced as it is in the simulation. On the other hand, due to the small number of filling particles, the load transfer through a coarse granular assemblage only involves a limited number of force chains, which results in inadequate contact points on relatively small sensor plates and makes the measurements highly variable in both experiment and simulation. Therefore, the difference between the numerical and experimental data of the transmitted force is expected, despite a closer match is observed for the distribution along the horizontal centerline, as shown in Fig. 11(b).

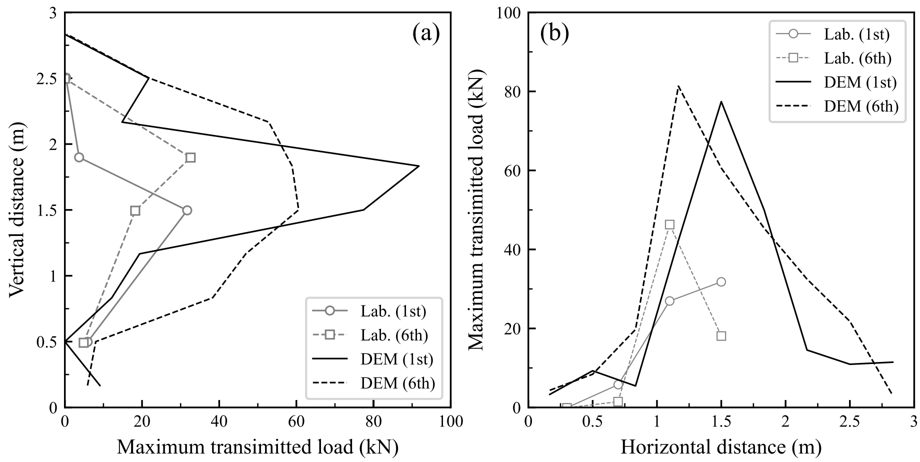

Fig. 11. Comparison between the numerical and experimental data regarding the spatial distribution of the maximum transmitted force for the first and the sixth impacts along (a) the vertical and (b) the horizontal centerlines when the impact energy is 20 kJ. The experimental data is measured by Ng et al. (2016).

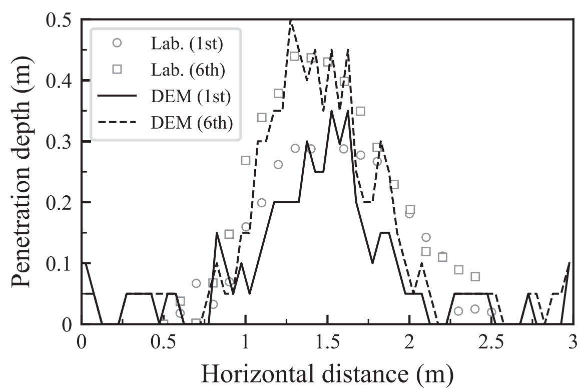

Fig. 12. Comparison between the numerical and experimental data regarding the distribution of the penetration depth for the first and the sixth impacts along the horizontal centerline when the impact energy is 20 kJ. The experimental data is measured by Ng et al. (2016).

3.3. Deformation of the gabion cushion layer

The deformation of the gabion cushion layer can be characterized by the penetration depth of the boulder (or the outline of the crater) after successive impacts, which is the key parameter to design the minimum thickness of the cushion layer in engineering practice. Fig. 12 compares the simulation and the experiment in terms of the spatial distribution of the penetration depth for the first and the sixth impacts along the horizontal centerline when the impact energy is 20 kJ. Surprisingly, the numerical results agree with the experimental measurements rather well. It is likely due to the fact that the deformation of the gabion cushion layer is less sensitive to the randomness caused by the small number of particles, unlike the impact force and the transmitted force. Fig. 12 shows that the edge of the crater spreads to a horizontal distance of 1 m from the center, which is about 1.7 times of the boulder radius. Also, the maximum penetration depth increases roughly from 0.35 m to 0.5 m during the first and the sixth impacts.

All in all, despite some differences in the specific value of a certain measurement, our DEM model can reproduce the general mechanical response of a rock filled gabion under successive boulder impacts.

4. Parametric study of gabion cushion performance

It is well known that the overall performance of a granular assembly is a collective behavior of inter-particle interactions at each individual contact. Up to now, it is still unclear how the contact properties could possibly affect the cushion performance of rock-filled gabions under successive boulder impacts. Besides, we are also interested in the dynamic impact behavior as the impact energy changes, which may alter the relative importance of friction, collision and particle crushing. Therefore, the validated DEM model is applied in this section to investigate the effects of contact properties (i.e. inter-particle friction coefficient and damping ratio) and impact energy on the performance of the gabion cushion layer.

4.1. Effects of contact properties

The effects of the inter-particle friction coefficient μ and the damping ratio β on the cushion performance of rock-filled gabions are investigated. Note that the inter-particle contact properties here refer to the properties of the constituent balls. The same value for the damping ratio in the calculation of normal and tangential contact force components is adopted. Generally speaking, increasing the friction coefficient μ increases the amount of energy dissipation whenever two particles slip at contact. Meanwhile, a higher friction coefficient also makes slippage more difficult to occur (Staron and Hinch, 2006). Therefore, the resultant effect (positive or negative) of increasing the friction coefficient on the energy dissipation rate of the whole granular assembly becomes uncertain. On the other hand, increasing the damping ratio (or equivalently decreasing the restitution coefficient) will lead to more energy dissipation during collisions.

Fig. 13 presents the influence of the friction coefficient μ on the peak impact force. The damping ratio β is fixed to be 0.1 and the impact energy is kept constant at 20 kJ. For large values of friction coefficient greater than 0.3, the influence on the peak impact force during the first and the sixth impacts is small. In contrast, as the friction coefficient decreases from 0.3 to 0.1, the peak impact forces during the first and the sixth impacts reduce significantly by 37.2% and 44.6%, respectively. When the damping ratio β increases to 0.5 and 0.9, see the symbols filled by the gray and black colors in Fig. 13, the peak impact force during the first and the sixth impacts decreases by 14.2% and 7.3%, respectively, to the utmost extent. It means that the influence of the damping ratio on the peak impact force is relatively small. Note that a β value of 0.1 results in a restitution coefficient of about 0.73, which is close to the property of quartz. Large β values are used to illustrate the largest possible influence of β on the gabion cushion performance, and a large β value is also associated with the large surface roughness of particles (Li et al., 2020). Interestingly, it is observed that the peak impact force increases from 158 kN to 170 kN during the first and the sixth impacts when the friction coefficient is 0.1 (i.e, only 7.8% increase), while a higher friction coefficient greater than 0.3 results in

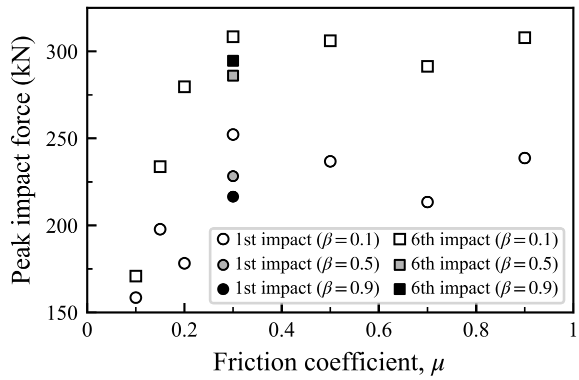

Fig. 13. Effects of the inter-particle friction coefficient on the peak impact force during the first and the sixth impacts. The impact energy is 20 kJ.

a minimum increase of 22.3%. It means that the function of the gabion cushion layer is well maintained during successive boulder impacts when the inter-particle friction coefficient is small.

The great influence of the friction coefficient on the peak impact force suggests that inter-particle friction is likely the dominant mechanism during successive boulder impacts, which can be confirmed by examining the relative importance of various sources of energy dissipation. In DEM simulations, the kinetic energy of the boulder E_{kb} can be calculated based on its velocity v, i.e., $E_{kb} = 0.5mv^2$. The initial kinetic energy of the boulder E_{k0} is the impact energy, which is also the total energy input to the whole system during each boulder impact. Here we ignore the kinetic energy of the wire mesh due to its small mass (only 0.12% of the filling particles), then the difference between the kinetic energy of the whole system at any moment and the boulder kinetic energy E_{kb} becomes the kinetic energy of the particles inside the gabion, which is denoted by E_{kp}. The total strain energy ($E_c = E_c^{\mathrm{linear}} + E_c^{\mathrm{bond}}$) can be calculated based on the overlaps between contacting particles and the deformations of the bonds, i.e., $E_c^{\mathrm{linear}} = 0.5(|\boldsymbol{F}_n^l|^2/k_n + |\boldsymbol{F}_t^l|^2/k_t)$ and $E_c^{\mathrm{bond}} = 0.5\left[|\bar{\boldsymbol{F}}_n|^2/(\bar{k}_n\bar{A}) + |\bar{\boldsymbol{F}}_t|^2/(\bar{k}_t\bar{A}) + |\bar{\boldsymbol{M}}_b|^2/(\bar{k}_n\bar{I}) + |\bar{\boldsymbol{M}}_t|^2/(\bar{k}_t\bar{J})\right]$, where E_c^{linear} and E_c^{bond} are the strain energies stored at the contacts and in the bonds, respectively. The linear component of the normal and tangential forces are denoted by $\boldsymbol{F}_n^l$ and $\boldsymbol{F}_t^l$. The bending and twisting moments are denoted by $\boldsymbol{M}_n^l$ and $\boldsymbol{M}_t^l$, respectively. The symbol $\bar{J}$ denotes the polar moment of inertia of the bond cross section. In PFC3D, the cumulative energy dissipations due to friction (E_{slip}) and collision (E_{damp}) are also tracked in an incremental manner, i.e., $\Delta E_{slip} = -0.5\boldsymbol{F}_t \cdot \delta_t^{\mu}$ and $\Delta E_{damp} = -\boldsymbol{F}_d \cdot (\dot{\boldsymbol{\delta}}\Delta t)$, where δ_t^{μ} is the slip displacement, $\boldsymbol{F}_d$ is the damping component of the contact forces in Eqs. (2) and (3), $\dot{\boldsymbol{\delta}}$ is the relative velocity at the contact and Δt is the time step. In this study, it is assumed that the energy loss due to the plastic deformation of the wire mesh, see Section 2.3, is negligible. And with the assumption of the energy conservation of the whole granular system, the energy dissipation due to particle crushing or breakage E_{crack} can be estimated as

$$E_{crack} = E_{k0} - E_{kb} - E_{kp} - E_c - E_{slip} - E_{damp}. \tag{7}$$

Note that E_{kp}, E_c, E_{slip} and E_{damp} in Eq. (7) represent the net changes to different forms of energy since the start of every impact event.

Fig. 14 compares the temporal evolution of different energies normalized by E_{k0}, i.e., 20 kJ, during the impact processes for different friction coefficients μ and damping ratios β. Let us first focus on the case when $\mu = 0.3$ and $\beta = 0.1$ for the general description of energy evolution, see Figs. 14(c) and 14(d), and the changes caused by varying μ and β will be discussed later. During the first impact, the boulder kinetic energy E_{kb} drops below 20% quickly within the first 0.05 s and then gradually drops to zero after 0.1 s, see Fig. 14(c). It agrees with the rapid increase and more gentle decrease of impact force, as shown in Fig. 10. Almost all the boulder kinetic energy is dissipated by friction, with the other energy dissipations maintained well below 4.5% during the whole impact process. At the end of the first impact, the total energy dissipation due to friction E_{slip} is as high as 90.2%. It is likely due to the fact that the gabion cushion layer is initially in a relatively loose state, allowing a high degree of particle rearrangement and thereby more slippage at contacts, which is evidenced by the significant kinetic energy of particles inside the gabion ($E_{kp} = 14.6\% E_{k0}$ at maximum).

During the sixth impact, as shown in Fig. 14(d), the boulder kinetic energy E_{kb} drops to zero at around $t = 0.06$ s. The shorter impact duration is directly associated with the larger impact force. In addition, there is a noticeable increase of the strain energy E_c, which reaches a maximum value of 14.8% at around $t = 0.05$ s. After that, the strain energy E_c is slowly released, transferring the energy back to the boulder. As a result, the boulder bounces back with a finite small kinetic energy (3.4% of E_{k0}), which is absent after the first impact. The energy dissipations due to collision E_{damp} and particle cracking E_{crack} also increase to 5.3% and 6.3%, respectively, after the sixth impact. In contrast, the kinetic energy of the particles inside the gabion E_{kp} quickly drops to zero and at the same time the energy dissipation due to friction E_{slip} saturates at around 81.5%. During successive boulder impacts, permanent plastic deformation gradually develops, forming a crater that reduces the effective thickness of the gabion cushion layer, as shown in Fig. 12. In the meantime, the crushed small fragments can fill the voids between the large particles, which further densifies the granular packing between the boulder and the rigid back wall (Su et al., 2021). The outcome is that less particle rearrangement is allowed and more energy is absorbed by collisions or the damping mechanism, bringing more severe particle cracking.

When the friction coefficient μ reduces to 0.1, the total energy dissipations due to friction E_{slip} after the first and the sixth impacts decrease to 76.0% and 63.9%, respectively, as shown in Figs. 14(a) and 14(b). Compared to the first impact, the response of different energies is delayed significantly during the sixth impact. For example, the peak kinetic energy of particles inside the gabion E_{kp} takes place before 0.05 s during the first impact and the same quantity occurs after 0.075 s during the sixth impact. It is mainly due to the formation of the crater and the boulder impacts the gabion cushion layer at a later stage. Also, the kinetic energy of particles inside the gabion E_{kp} increases significantly compared to the case when a higher friction coefficient $\mu = 0.3$ is adopted. It indicates that more particle rearrangements take place and the concentrated impact force can be diffused among a larger area, enhancing the overall cushion performance (Ng et al., 2016; Su et al., 2019).

When $\mu = 0.3$ and $\beta = 0.9$, the energy dissipations due to friction E_{slip} after the first and the sixth impacts are 85.6% and 76.1%, respectively, as shown in Figs. 14(e) and 14(f). These values are about 5% less than the corresponding quantities when the damping ratio β is as small as 0.1. The energy dissipation due to collision E_{damp} is almost doubled during successive boulder impacts when β increases from 0.1 to 0.9. However, it only covers 9.7% and 13.4% after the first and the sixth impacts, which are still much smaller than the energy dissipations due to friction. Note that a damping ratio as high as 0.9 (i.e., close to 0 restitution coefficient) is less realistic for the considered system, the associated numerical results are to demonstrate the limited energy dissipation due to the collision mechanism.

All in all, our DEM results clearly show that the dominant mechanism governing the successive boulder impacts on rock-filled gabions is inter-particle friction, instead of the more intuitionistic collision and particle cracking. This result supports the idea of using simplified DEM simulations by ignoring particle breakage (i.e., rigid spheres or clumps) to a certain extent (Bertrand et al., 2005; Su et al., 2019; Su and Choi, 2021; Nicot et al., 2007), as long as the frictional properties of the particles are well calibrated. Meanwhile, particle cracking in a granular system can induce force chain collapse and contribute to particle rearrangement (Tsoungui et al., 1999; Zhang et al., 2017),

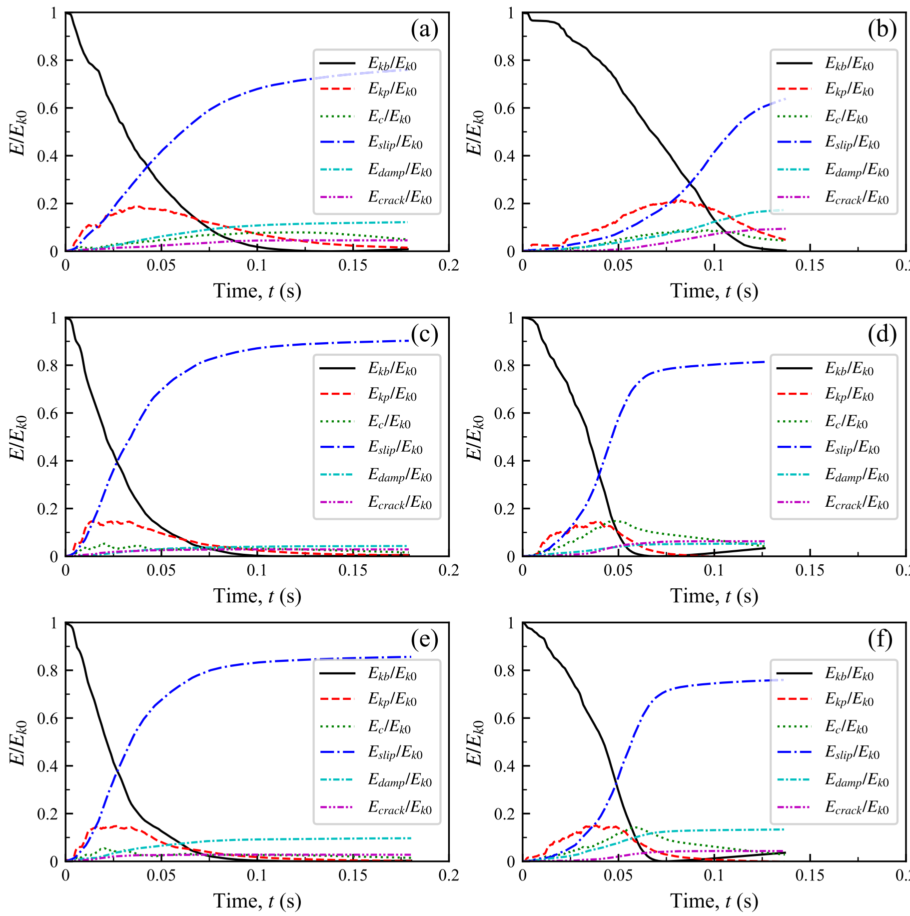

Fig. 14. Temporal evolution of the boulder kinetic energy E_{kb}, the kinetic energy of particles inside the gabion E_{kp}, the strain energy stored at contacts and in parallel bonds E_c, the energy dissipation due to friction or slippage E_{slip}, the energy dissipation due to collision or damping E_{damp}, and the energy dissipation due to particle cracking E_{crack}, normalized by the initial kinetic energy of the boulder E_{k0}, i.e., 20 kJ. (a, b) the first and sixth impacts with $\mu = 0.1$ and $\beta = 0.1$, (c, d) the first and sixth impacts with $\mu = 0.3$ and $\beta = 0.1$, (e, f) the first and sixth impacts with $\mu = 0.3$ and $\beta = 0.9$.

increasing the capacity of the granular system to deform under impact, and thereby reducing the impact force. Thus, even if dissipation by cracking is negligible, its potential effect on the overall impact response can still be significant.

4.2. Effects of impact energy

To investigate the effects of impact energy, a larger initial boulder velocity of 8.4 m/s is applied following the experiments (Ng et al., 2016). As a result, the impact energy increases from 20 kJ to 70 kJ. The inter-particle friction coefficient μ and the damping ratio β are kept constant at 0.3 and 0.1, respectively. Fig. 15 compares the two cases with different impact energies in terms of the peak impact force as the number of impacts increases. First of all, the peak impact force does not necessarily increase in a monotonic way during successive boulder impacts, probably due to the randomness caused by the limited number of particles and the particle arrangement (i.e., the granular packing) as mentioned in Section 3. However, a general increasing trend with the number of impacts can be observed. More specifically, when the impact energy is 20 kJ, the peak impact force increases from 252 kN to 308 kN after six impacts, i.e., 22.3% of increase. When the impact energy is 70 kJ, the peak impact force increases from 351 kN to 728 kN, which is more than doubled.

Fig. 16 compares the crater formation at different impact energies. At a low level of impact energy (20 kJ), there is only a small deformation of the gabion cushion layer taking place after the first impact, see Fig. 16(a), which agrees with the experimental observation (Ng et al., 2016). Note that it is not necessarily associated with a slight

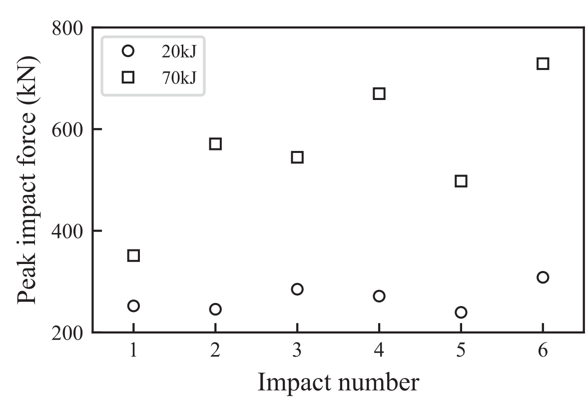

Fig. 15. Effects of the impact energy on the peak impact force during successive boulder impacts. The friction coefficient μ and the damping ratio β are set to be 0.3 and 0.1, respectively.

particle rearrangement during the impact process. Instead, the particle rearrangement is quite significant, as indicated by the noticeable particle kinetic energy E_{kp} in Fig. 14(c). A few wire mesh segments (in red) close to the center of the gabion cushion layer undergo plastic deformations. After the third impact, as shown in Fig. 16(b), an obvious crater is formed and the number of wire mesh segments with plastic deformations greatly increases. Also, local failure of the wire mesh can be observed, forming large openings through which the particles

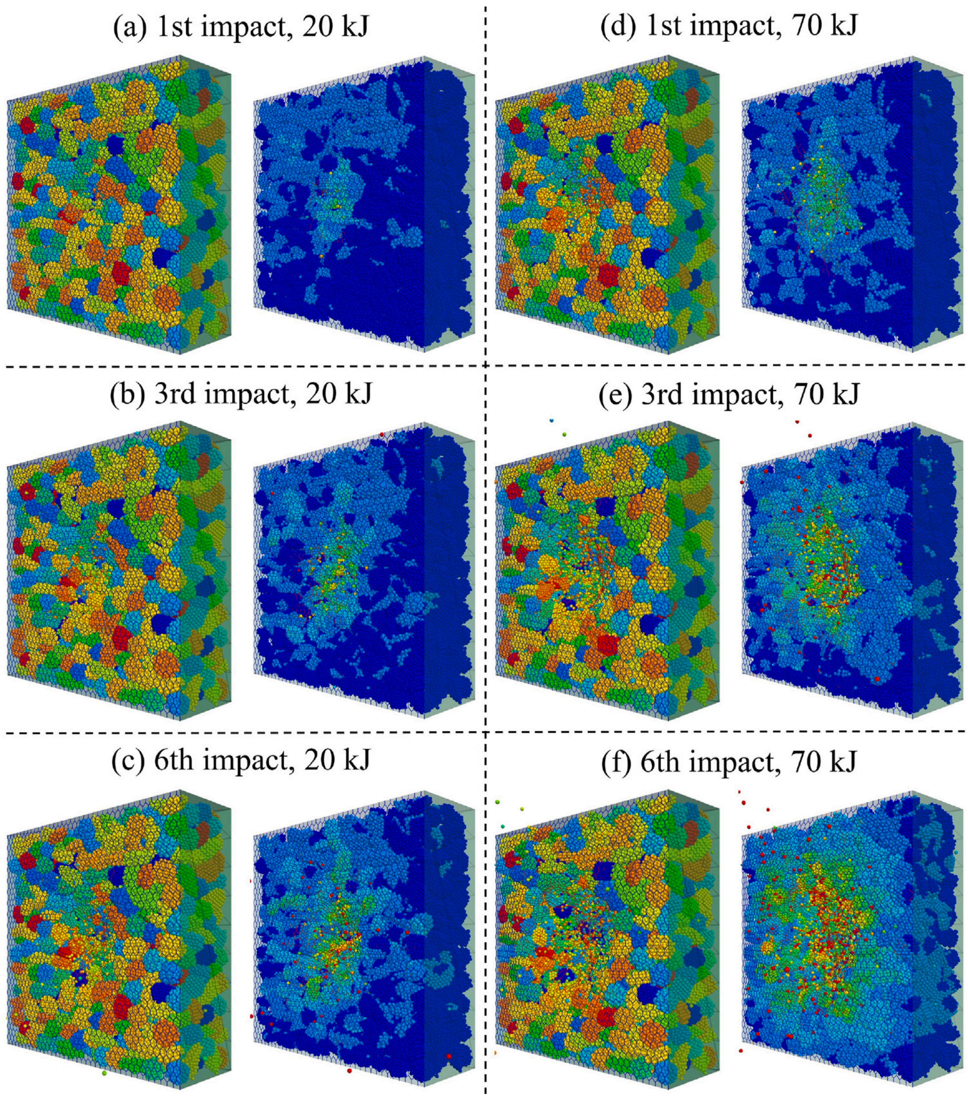

Fig. 16. Crater formation during successive boulder impacts. (a–c) craters after first, third and sixth impacts when the impact energy is 20 kJ, (d–f) craters after first, third and sixth impacts when the impact energy is 70 kJ. In each subplot, the balls are painted with the same color if they belong to the same particle or fragment on the left image and painted according to the displacement (blue to red as the displacement increases from 0 to 0.5 m) on the right image. The friction coefficient μ and the damping ratio β are set to be 0.3 and 0.1, respectively.

can pass. After the sixth impact, as shown in Fig. 16(c), the crater at the center becomes even larger. Almost all the wire mesh segments close to the center are in the softening state. The openings caused by the damage of the wire mesh segments further enlarge. In addition, significant particle crushing occurs and some small fragments fly out of the gabion cushion layer, which again qualitatively agrees with the experimental observation (Ng et al., 2016). In experiments, the metal wires in the impacted area could be cut due to the direct compression between the boulder and the filling particles in the direction perpendicular to the wire (Lambert et al., 2020). This wire cutting mechanism is not accounted for in the current DEM model, which requires further improvements to the modeling technique for breakable wire meshes.

When the impact energy increases to 70 kJ, a noticeable crater is formed after the very first impact, which is accompanied with large plastic deformations and local failures of the wire mesh, as shown in Fig. 16(d). After the third impact, the size of the crater is already larger than or at least comparable to that after six impacts at 20 kJ, see Figs. 16(c) and 16(e). The sixth impact at 70 kJ creates a large hole of the wire mesh close to the center, and more significant particle crushing is observed, as shown in Fig. 16(f). At this point, the gabion cushion layer is greatly damaged and repairing of the wire mesh basket becomes necessary if it is in experiments or in the field.

To gain a better understanding of the impact dynamics at 70 kJ, the temporal evolution of various normalized energies, the same as Fig. 14, is presented in Fig. 17. During the first impact, as shown in Fig. 17(a), the boulder kinetic energy E_{kb} gradually decreases in a nearly linear pattern. Before $t = 0.05$ s, about 12.4% of the boulder kinetic energy is transferred to the kinetic energy of the particles inside the gabion E_{kp}. The strain energy E_c and the energy dissipations due to collision E_{damp} or cracking E_{crack} only increase slightly. Almost all the boulder kinetic energy is dissipated via inter-particle friction E_{slip}. At the end of the first impact, the total energy dissipation due to friction is 87.6%, which is rather similar to the value (86%) predicted by the model from Su et al. (2019) in which particle crushing was ignored and a Hertz–Mindlin contact model was adopted. The final energy dissipation due to cracking E_{crack} is larger than that due to collision E_{damp}, which is different from the results when the impact energy is 20 kJ and is likely due to the more severe particle cracking, as shown in Fig. 16(d).

The energy evolution changes quite significantly during the sixth impact, as shown in Fig. 17(b). Most of the boulder kinetic energy E_{kb} is lost within a short period from 0.025 s to 0.05 s. The sudden drop of E_{kb} indicates large rate of momentum exchange, which is associated with the largely amplified impact force in Fig. 15. The rapid decrease

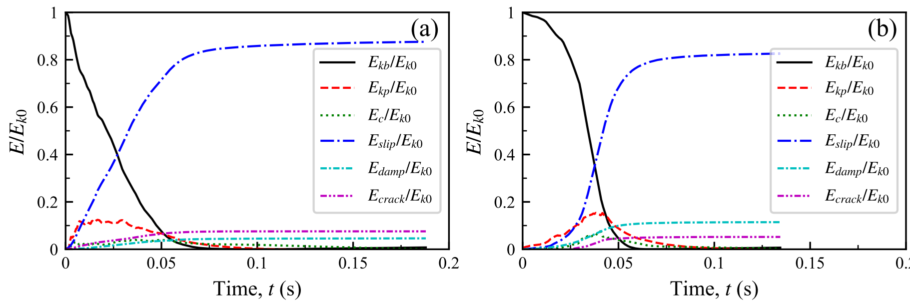

Fig. 17. Temporal evolution of various energies (see Fig. 14) normalized by the initial kinetic energy of the boulder E_{k0}, i.e., 70 kJ, during (a) the first impact and (b) the sixth impact. The friction coefficient μ and the damping ratio β are set to be 0.3 and 0.1, respectively.

of the particle kinetic energy E_{kp} after reaching the peak also indicates less particle rearrangements. As a result, the total energy dissipation due to friction E_{slip} reduces from 87.6% to 82.6%. In the meantime, the total energy dissipation due to collision E_{damp} increases from 4.6% to 11.4%.

Comparing the cases when the impact energy is 20 kJ and 70 kJ, we can observe a large difference regarding the strain energy stored at the contacts and in the bonds (E_c). When the impact energy increases, the energy dissipation due to collision also increases. As a result, the maximum strain energy E_c reduces from 14.8% to 7.6%, which is roughly halved. It is known that the strain energy is recoverable, and can be transferred back to the kinetic energy of the boulder, resulting in a bounce-back motion after the impact at 20 kJ, see Fig. 14(d). However, such a bounce-back behavior is absent when the impact energy increases to 70 kJ. In real debris flow events and flume tests where multiple boulders are present and impact the barrier successively, the bounce-back behavior of the boulders may affect the impact load significantly, just like the reflection waves (Ng et al., 2021), which should be properly considered in the design practice.

5. Concluding remarks

In this paper, we present discrete element simulations of rock-filled gabions under successive boulder impacts. A unique DEM model consisting of irregular crushable filling particles and a flexible wire mesh is established. The objective is to explicitly capture the irreversible plastic deformation of the gabion cushion layer and the potential damage of the wire mesh, which plays a vital role in the dynamic responses when multiple boulder impacts are considered. With the precise control of the input parameters (i.e., the inter-particle contact properties and the impact energy) and the additional information that can be extracted from DEM simulations, we are able to identify the governing mechanism during the impact processes at different energy levels.

The wire-node approach, combined with a soft bond contact model, is applied to simulate the wire mesh. To validate the model, a net punching test is simulated and the numerical result of force–displacement relationship is compared to the experimental measurement. A mesh sensitivity analysis is first carried out and it is found that the commonly adopted resolution with balls installed just at the nodes of the wire mesh produces a slightly stiffer response. The small influence of mesh resolution on the mechanical response of wire strands indicates that tension is the dominant loading pattern during the punching test and bending is a negligible mechanism. Also, compared to the parallel bond model, the soft bond model can better capture the mechanical responses of the wire mesh panel in terms of the reduced out-of-plane stiffness before failure.

To examine the performance of the DEM model for the rock-filled gabion, we have performed a one-to-one numerical simulation of the large-scale pendulum impact test carried out by Ng et al. (2016). The numerical results are compared to the experimental data regarding the boulder impact force, the transmitted load and the deformation of the gabion cushion layer after successive boulder impacts. A close agreement is observed, with a better match for the deformation. The larger differences between the numerical and experimental data for the forces are attributed to the high variability in measurements due to the limited number of particles and the small measuring area.

The validated DEM model is further applied to investigate the effects of contact properties and the impact energy on the cushion performance of rock-filled gabions. When the friction coefficient μ is less than 0.3, the peak impact force increases as μ increases. However, this positive relationship disappears when μ is larger than 0.3 and the effect of μ on the peak impact force becomes minor. Also, when μ is small (e.g., 0.1), the peak impact force during the sixth impact is only 7.8% larger than the value during the first impact, while a minimum increase of 22.3% is observed when μ is greater than 0.3. It means the cushion performance of the gabion filled with more frictional rock fragments deteriorates more quickly under successive boulder impacts. A close examination of the energy evolution suggests that less frictional particles have significant rearrangements even after multiple impacts, further reducing the impact force.

After six impacts, the peak impact force increases by 22.3% at 20 kJ but the same quantity is more than doubled at 70 kJ. The largely amplified force after multiple impacts at a higher energy level is associated with the reduced particle rearrangement and thereby a stiffer response. Furthermore, a bounce-back motion of the boulder is observed only when the impact energy is low, which may play a vital role in estimating the successive impact loads from multiple boulders in real debris flow events. Note that the impact energy is a function of both the landslide mobility and the flow composition, such as the boulder size. Therefore, it becomes rather important to combine techniques, including numerical simulation, case study and site investigation, for a better prediction of the impact energy so that the design of rock-filled gabions can be optimized.

CRediT authorship contribution statement

G.C. Yang: Writing – original draft, Software, Conceptualization. **F. Qiao:** Validation, Software, Methodology, Data curation. **Y. Lu:** Supervision, Resources. **Q.H. Yao:** Supervision, Project administration. **C.Y. Kwok:** Writing – review & editing.

Declaration of competing interest

The authors declare that they have no known competing financial interests or personal relationships that could have appeared to influence the work reported in this paper.

Data availability

Data will be made available on request.

Acknowledgments

This research is under the support of the NSFC project, China No. 42107154, the Hong Kong RGC project No. UGC/FDS13/E03/22, the Guangdong basic and applied basic research foundation projects No. 2020A1515110810 and No. 2023A1515012881, the Hong Kong GRF projects No. 17205821 and No. 17205222.

References

Albaba, A., Lambert, S., Kneib, F., Chareyre, B., Nicot, F., 2017. DEM modeling of a flexible barrier impacted by a dry granular flow. Rock Mech. Rock Eng. 50 (11), 3029–3048. http://dx.doi.org/10.1007/s00603-017-1286-z.

Bertrand, D., 2008. Numerical modelling of geocomposite cells designed for rockfall protection. Eur. J. Environ. Civ. Eng. 12 (3), 263–277. http://dx.doi.org/10.1080/19648189.2008.9693013.

Bertrand, D., Gotteland, P., Lambert, S., Nicot, F., Derache, F., 2006. Multi-scale modelling of cellular geo-composite structure under localized impact. Revue Européenne de Génie Civil 10 (3), 309–322. http://dx.doi.org/10.1080/17747120.2006.9692830.

Bertrand, D., Nicot, F., Gotteland, P., Lambert, S., 2005. Modelling a geo-composite cell using discrete analysis. Comput. Geotech. 32 (8), 564–577. http://dx.doi.org/10.1016/j.compgeo.2005.11.004.

Bertrand, D., Nicot, F., Gotteland, P., Lambert, S., 2008. Discrete element method (DEM) numerical modeling of double-twisted hexagonal mesh. Can. Geotech. J. 45 (8), 1104–1117. http://dx.doi.org/10.1139/t08-036.

Bolton, M.D., Nakata, Y., Cheng, Y.P., 2008. Micro- and macro-mechanical behaviour of DEM crushable materials. Géotechnique 58 (6), 471–480. http://dx.doi.org/10.1680/geot.2008.58.6.471.

Bourrier, F., Kneib, F., Chareyre, B., Fourcaud, T., 2013. Discrete modeling of granular soils reinforcement by plant roots. Ecol. Eng. 61, 646–657. http://dx.doi.org/10.1016/j.ecoleng.2013.05.002.

Bourrier, F., Lambert, S., Heymann, A., Gotteland, P., Nicot, F., 2011. How multi-scale approaches can benefit the design of cellular rockfall protection structures. Can. Geotech. J. 48 (12), 1803–1816. http://dx.doi.org/10.1139/t11-072.

Breugnot, A., Lambert, S., Villard, P., Gotteland, P., 2016. A discrete/continuous coupled approach for modeling impacts on cellular geostructures. Rock Mech. Rock Eng. 49 (5), 1831–1848. http://dx.doi.org/10.1007/s00603-015-0886-8.

Brocato, M., 2020. A continuum model of close packing granular materials for the study of rock filled gabions. Int. J. Solids Struct. 187, 38–47. http://dx.doi.org/10.1016/j.ijsolstr.2018.08.008.

Cheng, Y.P., Nakata, Y., Bolton, M.D., 2003. Discrete element simulation of crushable soil. Géotechnique 53 (7), 633–641. http://dx.doi.org/10.1680/geot.2003.53.7.633.

Coelho, R.M., Alves de Sousa, R.J., Fernandes, F.A.O., Teixeira-Dias, F., 2013. New composite liners for energy absorption purposes. Mater. Des. 43, 384–392. http://dx.doi.org/10.1016/j.matdes.2012.07.020.

Cundall, P.A., Strack, O.D.L., 1979. A discrete numerical model for granular assemblies. Géotechnique 29 (1), 47–65. http://dx.doi.org/10.1680/geot.1979.29.1.47.

de Bono, J.P., McDowell, G.R., 2016. Investigating the effects of particle shape on normal compression and overconsolidation using DEM. Granul. Matter 18 (3), 55. http://dx.doi.org/10.1007/s10035-016-0605-5.

Effeindzourou, A., Thoeni, K., Giacomini, A., Wendeler, C., 2017. Efficient discrete modelling of composite structures for rockfall protection. Comput. Geotech. 87, 99–114. http://dx.doi.org/10.1016/j.compgeo.2017.02.005.

GEO, 1993. Guide to Retaining Wall Design, Geoguide, 1. Technical Report, Geotechnical Engineering Office Hong Kong.

Heymann, A., Lambert, S., Haza-Rozier, E., Vinceslas, G., Gotteland, P., 2010. An experimental comparison of half-scale rockfall protection sandwich structures. In: 11th International Conference on Structures under Shock and Impact. WIT Press, pp. 15–26. http://dx.doi.org/10.2495/SU100021.

Huang, Y., Zhang, B., 2022. Challenges and perspectives in designing engineering structures against debris-flow disaster. Eur. J. Environ. Civ. Eng. 26 (10), 4476–4497. http://dx.doi.org/10.1080/19648189.2020.1854126.

Hübl, J., Suda, J., Proske, D., Kaitna, R., Scheidl, C., 2009. Debris flow impact estimation. In: Proceedings of the 11th International Symposium on Water Management and Hydraulic Engineering. Vol. 1. University od Ss Cyril and Methodius, Faculty of Civil Engineering, Skopje, Macedonia, pp. 137–148.

Iverson, R.M., 1997. The physics of debris flows. Rev. Geophys. 35 (3), 245–296. http://dx.doi.org/10.1029/97RG00426.

Johnson, C.G., Kokelaar, B.P., Iverson, R.M., Logan, M., LaHusen, R.G., Gray, J.M.N.T., 2012. Grain-size segregation and levee formation in geophysical mass flows. J. Geophys. Res.: Earth Surface 117 (F1), http://dx.doi.org/10.1029/2011jf002185.

Lambert, S., Bourrier, F., Gotteland, P., Nicot, F., 2020. An experimental investigation of the response of slender protective structures to rockfall impacts. Can. Geotech. J. 57 (8), 1215–1231. http://dx.doi.org/10.1139/cgj-2019-0147.

Lambert, S., Gotteland, P., Nicot, F., 2009. Experimental study of the impact response of geocells as components of rockfall protection embankments. Nat. Hazards Earth Syst. Sci. 9 (2), 459–467. http://dx.doi.org/10.5194/nhess-9-459-2009.

Lambert, S., Heymann, A., Gotteland, P., Nicot, F., 2014. Real-scale investigation of the kinematic response of a rockfall protection embankment. Nat. Hazards Earth Syst. Sci. 14 (5), 1269–1281. http://dx.doi.org/10.5194/nhess-14-1269-2014.

Li, X., Dong, M., Jiang, D., Li, S., Shang, Y., 2020. The effect of surface roughness on normal restitution coefficient, adhesion force and friction coefficient of the particle-wall collision. Powder Technol. 362, 17–25. http://dx.doi.org/10.1016/j.powtec.2019.11.120.

Li, X., Zhao, J., 2018. A unified CFD-DEM approach for modeling of debris flow impacts on flexible barriers. Int. J. Numer. Anal. Methods Geomech. 42 (14), 1643–1670. http://dx.doi.org/10.1002/nag.2806.

Ma, Y., Huang, H., 2018. DEM analysis of failure mechanisms in the intact Brazilian test. Int. J. Rock Mech. Min. Sci. 102, 109–119. http://dx.doi.org/10.1016/j.ijrmms.2017.11.010.

Marigo, N., Gabrieli, F., Pol, A., Bisson, A., Brezzi, L., 2021. A discrete element framework for the modelling of rock-filled gabions. IOP Conf. Ser.: Earth Environ. Sci. 833 (1), 012102. http://dx.doi.org/10.1088/1755-1315/833/1/012102.

McDowell, G.R., Harireche, O., 2002. Discrete element modelling of soil particle fracture. Géotechnique 52 (2), 131–135. http://dx.doi.org/10.1680/geot.2002.52.2.131.

Ng, C.W.W., Choi, C.E., Su, A.Y., Kwan, J.S.H., Lam, C., 2016. Large-scale successive boulder impacts on a rigid barrier shielded by gabions. Can. Geotech. J. 53 (10), 1688–1699. http://dx.doi.org/10.1139/cgj-2016-0073.

Ng, C.W.W., Liu, H., Choi, C.E., Kwan, J.S.H., Pun, W.K., 2021. Impact dynamics of boulder-enriched debris flow on a rigid barrier. J. Geotech. Geoenviron. Eng. 147 (3), 04021004. http://dx.doi.org/10.1061/(ASCE)GT.1943-5606.0002485.

Nicot, F., Gotteland, P., Bertrand, D., Lambert, S., 2007. Multiscale approach to geo-composite cellular structures subjected to rock impacts. Int. J. Numer. Anal. Methods Geomech. 31 (13), 1477–1515. http://dx.doi.org/10.1002/nag.604.

Perera, J.S., Lam, N., 2023. Rockfall protection wall that can withstand multiple strikes without needing to be repaired. Int. J. Impact Eng. 173, 104476. http://dx.doi.org/10.1016/j.ijimpeng.2022.104476.

Perera, J.S., Lam, N., Disfani, M.M., Gad, E., 2021. Experimental and analytical investigation of a RC wall with a gabion cushion subjected to boulder impact. Int. J. Impact Eng. 151, 103823. http://dx.doi.org/10.1016/j.ijimpeng.2021.103823.

Pol, A., Gabrieli, F., Brezzi, L., 2021. Discrete element analysis of the punching behaviour of a secured drapery system: from laboratory characterization to idealized in situ conditions. Acta Geotech. 16 (8), 2553–2573. http://dx.doi.org/10.1007/s11440-020-01119-z.

Potyondy, D.O., Cundall, P.A., 2004. A bonded-particle model for rock. Int. J. Rock Mech. Min. Sci. 41 (8), 1329–1364. http://dx.doi.org/10.1016/j.ijrmms.2004.09.011.

Previtali, M., Ciantia, M., Castellanza, R., Crosta, G., 2020. Mesh sensitivity in discrete element simulation of flexible protection structures. In: Conference Contribution. Loughborough University, pp. 1–4. http://dx.doi.org/10.17028/rd.lboro.12102534.v1.

Staron, L., Hinch, E.J., 2006. The spreading of a granular mass: role of grain properties and initial conditions. Granul. Matter 9 (3), 205. http://dx.doi.org/10.1007/s10035-006-0033-z.

Su, Y., Choi, C.E., 2021. Effects of particle shape on the cushioning mechanics of rock-filled gabions. Acta Geotech. 16 (4), 1043–1052. http://dx.doi.org/10.1007/s11440-020-01080-x.

Su, Y., Choi, C.E., Lv, Y.R., Wang, Y., Li, X., 2021. Towards realistic simulations of the impact dynamics of boulders on rock-filled gabion: Combineds effects of rock shapes and their crushing strength. Eng. Geol. 283, 106026. http://dx.doi.org/10.1016/j.enggeo.2021.106026.

Su, Y., Cui, Y., Ng, C., Choi, C., Kwan, J., 2019. Effects of particle size and cushioning thickness on the performance of rock-filled gabions used in protection against boulder impact. Can. Geotech. J. 56 (2), 198–207. http://dx.doi.org/10.1139/cgj-2017-0370.

Thoeni, K., Lambert, C., Giacomini, A., Sloan, S.W., 2013. Discrete modelling of hexagonal wire meshes with a stochastically distorted contact model. Comput. Geotech. 49, 158–169. http://dx.doi.org/10.1016/j.compgeo.2012.10.014.

Tsoungui, O., Vallet, D., Charmet, J.-C., 1999. Numerical model of crushing of grains inside two-dimensional granular materials. Powder Technol. 105 (1), 190–198. http://dx.doi.org/10.1016/S0032-5910(99)00137-0.

Vagnon, F., 2020. Design of active debris flow mitigation measures: a comprehensive analysis of existing impact models. Landslides 17 (2), 313–333. http://dx.doi.org/10.1007/s10346-019-01278-5.

Volkwein, A., Wendeler, C., Guasti, G., 2011. Design of flexible debris flow barriers. Italian J. Eng. Geol. Environ. 1093–1100. http://dx.doi.org/10.4408/IJEGE.2011-03.B-118.

Yan, Y., Tang, H., Hu, K., Turowski, J.M., Wei, F., 2023. Deriving debris-flow dynamics from real-time impact-force measurements. J. Geophys. Res.: Earth Surface 128 (3), http://dx.doi.org/10.1029/2022JF006715, e2022JF006715.

Zhang, L., Nguyen, N.G.H., Lambert, S., Nicot, F., Prunier, F., Djeran-Maigre, I., 2017. The role of force chains in granular materials: from statics to dynamics. Eur. J. Environ. Civ. Eng. 21 (7–8), 874–895. http://dx.doi.org/10.1080/19648189.2016.1194332.